

Surveys of clumps, cores, and condensations in Cygnus-X: Searching for circumstellar disks

Xing Pan^{1,2}, Keping Qiu^{1,2}, Kai Yang^{1,2}, Yue Cao^{1,2}, Xu Zhang^{1,2}

¹ School of Astronomy and Space Science, Nanjing University, 163 Xianlin Avenue, Nanjing 210023, P.R.China
e-mail: kpqiu@nju.edu.cn

² Key Laboratory of Modern Astronomy and Astrophysics (Nanjing University), Ministry of Education, Nanjing 210023, P.R.China

January 1, 2024

ABSTRACT

Context. Theories and models have suggested that circumstellar disks could channel material to the central protostar, and resist star formation feedback. Our current knowledge of the picture and role of disks around massive protostars is unclear because the observational evidence of these circumstellar disks is limited.

Aims. To investigate whether disk-mediated accretion is the primary mechanism in high-mass star formation, we have established a survey of a large sample of massive dense cores within a giant molecular cloud.

Methods. We used high angular resolution ($\sim 1.8''$) observations with SMA to study the dust emission and molecular line emission of about 50 massive dense cores in Cygnus-X. At a typical distance of 1.4 kpc for Cygnus-X, these massive dense cores are resolved into ~ 2000 au condensations. We combined the CO outflow emission and gas kinematics traced by several high-density tracers to search for disk candidates.

Results. We extracted hundreds of dust condensations from the SMA 1.3 mm dust continuum emission. The CO data show bipolar or unipolar outflow signatures toward 49 dust condensations. Among them, only 27 sources are detected in dense gas tracers, which reveals the gas kinematics, and nine sources show evidence of rotating envelopes, suggesting the existence of embedded accretion disks. The position-velocity diagrams along the velocity gradient of all rotating condensations suggest that four condensations are possible to host Keplerian-like disks.

Conclusions. A detailed investigation of the 27 sources detected in dense gas tracers suggests that the nine disk candidates are at earlier evolutionary stages compared to the remaining 18 sources. Non-detection of rotating disks in our sample may be due to several factors, including an unknown inclination angle of the rotation axis and an early evolutionary stage of the central source, and the latter could be important, considering that young and powerful outflows could confuse the observational evidence for rotation. The detection rate of disk candidates in our sample is 1/3, which confirms that disk accretion is a viable mechanism for high-mass star formation, although it may not be the only one.

Key words. stars:massive - accretion, accretion disks - ISM:jets and outflows - ISM:kinematics and dynamics

1. Introduction

Before being confirmed through observations, disks have been expected to surround forming stars of different masses since, under the conservation of angular momentum, the collapsing cloud will flatten perpendicular to the rotation axis. Numerical models (Klassen et al. 2016; Rosen et al. 2016; Harries et al. 2017; Meyer et al. 2018) have also suggested that circumstellar disks can channel material to the central forming star, overcoming the strong feedback from the central protostar that may halt the infall of material (Kahn 1974; Wolfire & Cassinelli 1987). Circumstellar disks around low- ($M_* < 2M_\odot$) and intermediate-mass ($2M_\odot < M_* < 8M_\odot$) protostars have often been detected (e.g., Ansdell et al. 2016, 2018; Tripathi et al. 2017; Andrews et al. 2018). However, the picture and role of the circumstellar disks around high-mass protostars ($M_* > 8M_\odot$) are still unclear. Observational difficulties arise as they are relatively rare, distant (the typical distance is several kpc), and embedded in more crowded environments than their low-mass counterparts. In many cases, complex velocity structures and potential multiplicity can also confuse the detection (e.g., Cesaroni et al. 2017;

Ahmadi et al. 2018; Beuther et al. 2018). Additionally, the commonly insufficient angular resolution makes confirming the existence of disks around massive protostars a challenging task.

Searching for disks around massive stars with (sub)mm interferometers can be dated back to the late 1990s (Zhang et al. 1998). Despite the aforementioned limitations, there is accumulating evidence for disks around high-mass protostars (Wang et al. 2012; Sánchez-Monge et al. 2013; Cesaroni et al. 2014; Beltrán et al. 2014; Beltrán & de Wit 2016; Girart et al. 2017), thanks to instrument development. With the advent of the Atacama Large Millimeter Array (ALMA), which has sufficiently high angular resolutions ($< 0.1''$, corresponding to ≤ 100 au at a typical distance of a few kpc for high-mass star-forming regions) and a high sensitivity, evidence for Keplerian rotating disks around massive protostars has been found, such as G35.20-0.74N (Sánchez-Monge et al. 2013), G35.03+0.35 (Beltrán et al. 2014), Orion source I (Ginsburg et al. 2018), G17.64+0.16 (Maud et al. 2018), G11.92-0.61 MM1 (Ilee et al. 2018), and MonR2-IRS2 (Jiménez-Serra et al. 2020). Despite the growing observational evidence of Keplerian disks (on the order of $10^2 \sim 10^3$ au), there are also some studies that found no

disks at similar resolutions (Ginsburg et al. 2017; Goddi et al. 2020). Considering the limited sample size of detection and non-detection cases, it is still uncertain whether the disk-mediated accretion scenario is the primary mechanism for high-mass star formation.

With this in mind, we use the Submillimeter Array (SMA) to build a large sample of disk candidates in Cygnus-X at 1.3 mm with multiple configurations. Cygnus-X is the most massive giant molecular cloud within 3 kpc of the Sun (Schneider et al. 2006). It also has a rich collection of HII regions (Wendker et al. 1991) and several OB associations (Uyaniker et al. 2001), making it an active star formation region in the Galaxy. Hundreds of massive dense cores (the size of a few 0.1 pc, masses of tens to hundreds of Solar masses) have been identified in the complex (Motte et al. 2007; Cao et al. 2019). Previous observations (e.g., Bontemps et al. 2010) with high angular resolutions have resolved some of these dense cores into smaller fragments on the order of 1000 au, which are termed condensations. We conducted an SMA survey of dust continuum and molecular line emission in 1.3 mm toward 48 massive dense cores identified in Cygnus-X. With a resolution of 1.8" (corresponding to ~ 2000 au at a distance of 1.4 kpc for Cygnus-X), we find a large population of dust condensations. As a part of our project, Surveys of Clumps, CorEs, and CoNdenSations in CygnUS-X (CENSUS, PI: Keping Qiu), this paper focuses on the outflow structures and gas kinematics around the dust condensations. Our SMA survey reveals many CO outflows originating in condensations. High-density tracers (e.g., CH₃CN, CH₃OH and H₂CO lines) have allowed us to further investigate the molecular gas kinematics of the condensations. This paper is structured as follows. Section 2 summarizes the observations and data reduction. Section 3 presents the images of 1.3 mm dust continuum, outflows, and the velocity field traced by selected molecular lines along with the derived gas temperature. In Section 4, we provide the detection rate and its implications for high-mass star formation. Summaries are presented in Section 5.

2. Observations and data reduction

We first chose massive dense cores (MDCs) identified by Motte et al. (2007) as the targets of the SMA high-resolution observations. Because the region toward Cygnus OB2 was not covered by Motte et al. (2007), we then added eight dust continuum peaks seen in the JCMT 850 μ m maps of the OB2 region Cao et al. (2019). Since we are searching for disk candidates toward dust condensations in this work, we excluded the SMA data that detected no dust condensations or for which the 1.3 mm continuum emission was heavily contaminated by the free-free emission. In the end, the SMA observations presented in this work were done with 31 single-pointing fields and two mosaic fields, covering 48 MDCs identified by Cao et al. (2021) (see Table A.1). It is also worth noting that all these MDCs were included in a VLA study of compact radio sources by Wang et al. (2022), which is also part of the CENSUS project. Detailed information about our SMA observations is presented in Table 1.

We calibrated the raw data with the IDL superset MIR¹, and exported the calibrated visibilities into CASA (McMullin et al. 2007) for joint imaging. All images were made using a Briggs weighting of 0.5 (Briggs 1995) to balance resolution and sensitivity. The resulting synthesized beams are $\sim 1.8''$ in the final maps. During our observations, the SMA correlator was being upgraded from the ASIC to SWARM. Also considering the

archive observations, the data used in this project had total bandwidths ranging from 4 GHz to 16 GHz, and the spectral resolution also varied. However, all the high-density tracers relevant to this work and the outflow tracers, CO (2-1), ¹³CO (2-1), and SiO (5-4), were all covered by each observation. We also smoothed all the data into a uniform-frequency resolution of 812.5 kHz (~ 1 km s⁻¹ at 230 GHz) during imaging.

3. Results

3.1. Dust condensations and outflows

The 1.3 mm continuum maps of sources in our sample are shown in Fig 1 (Fig A.1 and Fig A.3 show continuum maps of the two mosaic fields). With a typical resolution of $\sim 1.8''$ (~ 2000 au), these massive dense cores (MDCs, ~ 0.1 pc) are resolved into dust condensations (~ 0.01 pc). Most fields harbor a few bright and compact condensations, except Field15, which appears to be dominated by a single source. Some fields, such as Field2 and Field17, exhibit high levels of fragmentation. Cao et al. (2021) employed “*getsources*”² to identify condensation from these MDCs. Applying the criterion that the emission peak must exceed 5σ of the image noise levels, the robust detections of dust condensations are about 200. The full width at half maximum (FWHM) diameters of these condensations range from 0.008 to 0.05 pc.

To search for disk candidates, first we have to find condensations located at the geometrical center of a bipolar outflow or connected to a unipolar outflow, since accretion disks are expected to be associated with jets or outflows ejected along their rotation axes (Cesaroni et al. 2007). CO emission lines usually trace the molecular outflowing gas. The velocity-integrated intensity maps of ¹²CO 2 – 1 toward sources in our sample are shown in Fig 2 (Fig A.2 and Fig A.4 show outflow structures of the two mosaic fields). We use red and blue arrows to depict redshifted and blueshifted outflow axes, respectively. SiO 5 – 4 emission also help us confirm the outflow axis. The details of the SiO 5 – 4 emission are presented in Yang et al. (2023). In total, we find 49 dust condensations associated with outflows (hereafter “outflow-associated” condensations) and expect to find disk candidates among them.

3.2. High-density tracers

The most reliable criteria of disk identification are based on the velocity field, which requires us to study the kinematics of these 49 outflow-associated condensations. We looked through all the detected molecular line emission from outflow-associated condensations and found that only 27 of these condensations have high-density tracers to investigate the kinematics. These 27 condensations are labeled as “dense-gas-traced.” For the other 22 outflow-associated condensations, we cannot study their kinematics, and therefore we leave them out in the following analyses.

We detect a series of molecular lines tracing high-density gas for each dense-gas-traced condensation, including transitions from CH₃CN, CH₃OH, H₂CO, and DCN. The information on these transitions is listed in Table 2. CH₃CN lines have proven to be a great dense gas and disk tracer. However, we only detect

² A powerful multi-scale, multi-wavelength source extraction algorithm Men’shchikov et al. (2012). “*getsources*” is designed for extracting dense structures in star-forming regions, decomposing images into components and measuring their properties by removing the large-scale background.

¹ <https://lweb.cfa.harvard.edu/~cqi/mircook.html>

Table 1. List of observational parameters

Observation Date	Array Configuration	N_{Ant}^a	Bandpass Calibrator	Gain Calibrator	Flux Calibrator	Observation ^b Field
2011/05/31	Compact	7	3C279	MWC349a	Titan	33
2011/06/03	Compact	8	3C279	MWC349a	Titan/Uranus	33
2011/06/27	Subcompact	7	3C279	MWC349a	Titan/Uranus	33
2012/07/08	Compact	6	3C279	MWC349a	Uranus	32
2012/08/03	Subcompact	6	3C279	MWC349a	Titan/Mars	32
2012/08/16	Subcompact	5	3C279	MWC349a	Saturn	32
2015/06/14	Compact	7	3C84	MWC349a	Neptune	1/2/3/4
2015/06/16	Compact	7	3C84	MWC349a	Neptune/Uranus	21/22/23/24
2015/06/18	Compact	7	3C454.3	MWC349a	Neptune	6/7/8
2015/07/05	Compact	6	3C279	MWC349a	Neptune	1/2/3/4
2015/07/06	Compact	6	3C454.3	MWC349a	Neptune	6/7/8
2015/07/07	Compact	6	3C454.3	MWC349a	Neptune	9/10/11/12/17
2015/07/14	Compact	6	3C279	MWC349a	Uranus	13/14/25
2015/07/18	Compact	6	3C279	MWC349a	Neptune	9/10/11/12/17
2015/07/19	Compact	6	3C279	MWC349a	Neptune	13/14/16/25
2015/07/26	Compact	6	3C279/3C454.3	MWC349a	Titan	5/18/19/20
2015/08/02	Compact	5	3C454.3	MWC349a	Neptune	21/22/23/24
2015/08/09	Compact	6	3C454.3	MWC349a	Neptune	21/22/23/24
2015/09/18	Extended	7	3C454.3	MWC349a	Neptune	13/14/16/23/24/25
2015/09/24	Extended	7	3C454.3	MWC349a	Neptune/Uranus	17/18/19/20/21/22
2015/09/25	Extended	7	3C454.3	MWC349a	Neptune/Uranus	8/9/10/11/12
2015/10/02	Extended	7	3C454.3	MWC349a	Neptune	1/2/3/4/5/6/7
2015/10/03	Extended	7	3C454.3	MWC349a	Neptune/Uranus	8/9/10/11/12
2015/10/07	Extended	7	3C454.3	MWC349a	Neptune/Uranus	8/9/10/11/12
2015/10/21	Subcompact	6	3C454.3	MWC349a	Uranus	1/2/3/9/10/15
2015/10/22	Subcompact	6	3C454.3	MWC349a	Uranus	8/13/14/20/23
2015/10/28	Subcompact	7	3C454.3	MWC349a	Uranus	11/12/15/16
2015/11/01	Subcompact	7	3C454.3	MWC349a	Neptune	1/2/3/4/5/6/7/8/9/10
2015/11/04	Subcompact	7	3C454.3	MWC349a	Uranus	13/14/17/18/19/20/21/22/23/24/25
2016/07/15	Very Extended	8	3C454.3	MWC349a	Neptune	9/16/22/32
2016/07/29	Very Extended	8	3C273	MWC349a	Titan	33
2016/08/16	Subcompact	6	3C279	MWC349a	Neptune	15/19
2016/08/25	Subcompact	8	3C279/3C454.3	MWC349a	Neptune	26/27/28/29/30/31
2016/10/06	Extended	7	3C454.3	MWC349a	Neptune	33
2016/11/22	Extended	8	3C84	MWC349a	Neptune	1/2/3/4/5/8/9/10/11/12
2016/11/23	Extended	8	3C84	MWC349a	Neptune	17/18/20/21/23/25

Notes.^(a) Number of available antennae in each observation.^(b) ID of Field from Table A.1 covered in each observation.

CH₃CN emission in a few sources. Considering the various evolutionary stages and physical and chemical properties of condensations in our sample, it is difficult to find a uniform disk tracer for all the condensations. Consequently, we employed different species to investigate the kinematics in our study. The intensity-weighted mean velocity (first-moment) maps of the representative molecular line toward dense-gas-traced condensations are shown in Fig 3. We chose the molecular spectral lines to show the dense gas kinematics according to the following criteria: (i) the molecular line should show compact emission around the central source of the outflow, which ensures the emission mainly come from the circumstellar disk or surrounding envelope; (ii) if several dense gas tracers all exhibited a velocity gradient in a similar direction, we chose the molecular line whose emission exhibited the clearest velocity gradient. In most cases, we had seven molecular line emission from five species to investigate the kinematics of these dense-gas-traced condensations. The high-excitation transitions of CH₃CN and CH₃OH are common dense

gas tracers to search for rotating disks or “toroids.” The line emission from low energy levels of some molecular species, DCN and H₂CO, can also trace the velocity fields around condensation. In some cases (e.g., Tobin et al. 2020; Cheng et al. 2022, Field8 MM1 in our sample), C¹⁸O (2-1) emission can also exhibit a velocity gradient as the result of a rotating disk or envelope.

3.3. Identification of disk candidates

The rotating disk candidates can be identified by two simple criteria following Cesaroni et al. (2017): (i) the position angle of the observed velocity gradient should be within 20° orthogonal to the CO outflow axis and (ii) the relative velocity with respect to the systemic velocity of the source should increase toward the center in the position-velocity (PV) plots. The position angles of the outflow axis and velocity gradient are given in Table 3. We

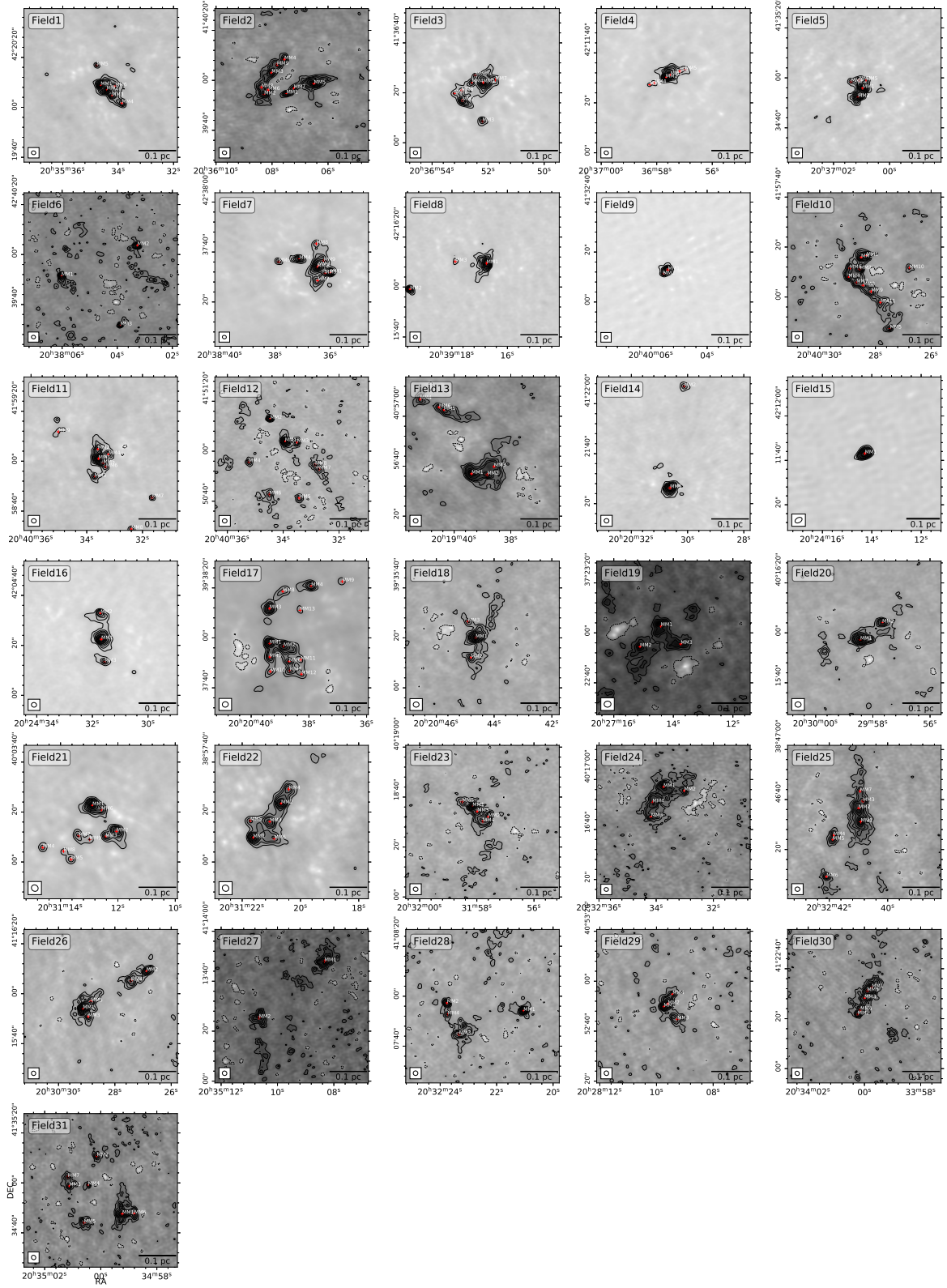


Fig. 1. SMA 1.3 mm continuum emission of sources in our sample. The contour levels are $(-3, 3, 6, 9, 12, 18, 24, 36, 48, 60) \times \sigma$, where σ is the rms of the dust continuum. The synthesized beam of each image is shown in the bottom left. The red plus represents the dust condensation extracted by Cao et al. (2021).

employ relatively loose constraints (20 degrees) on the relative angles between the outflow axis and velocity gradient for several reasons. First, the position angles of the outflow axis and velocity gradient are generally defined by eyes. The complex velocity

fields and asymmetries in the outflow emission can bring large uncertainties to the measurement of the position angles. Second, in some cases the dust condensations are clustered, making it difficult to confirm which one is the central source of the out-

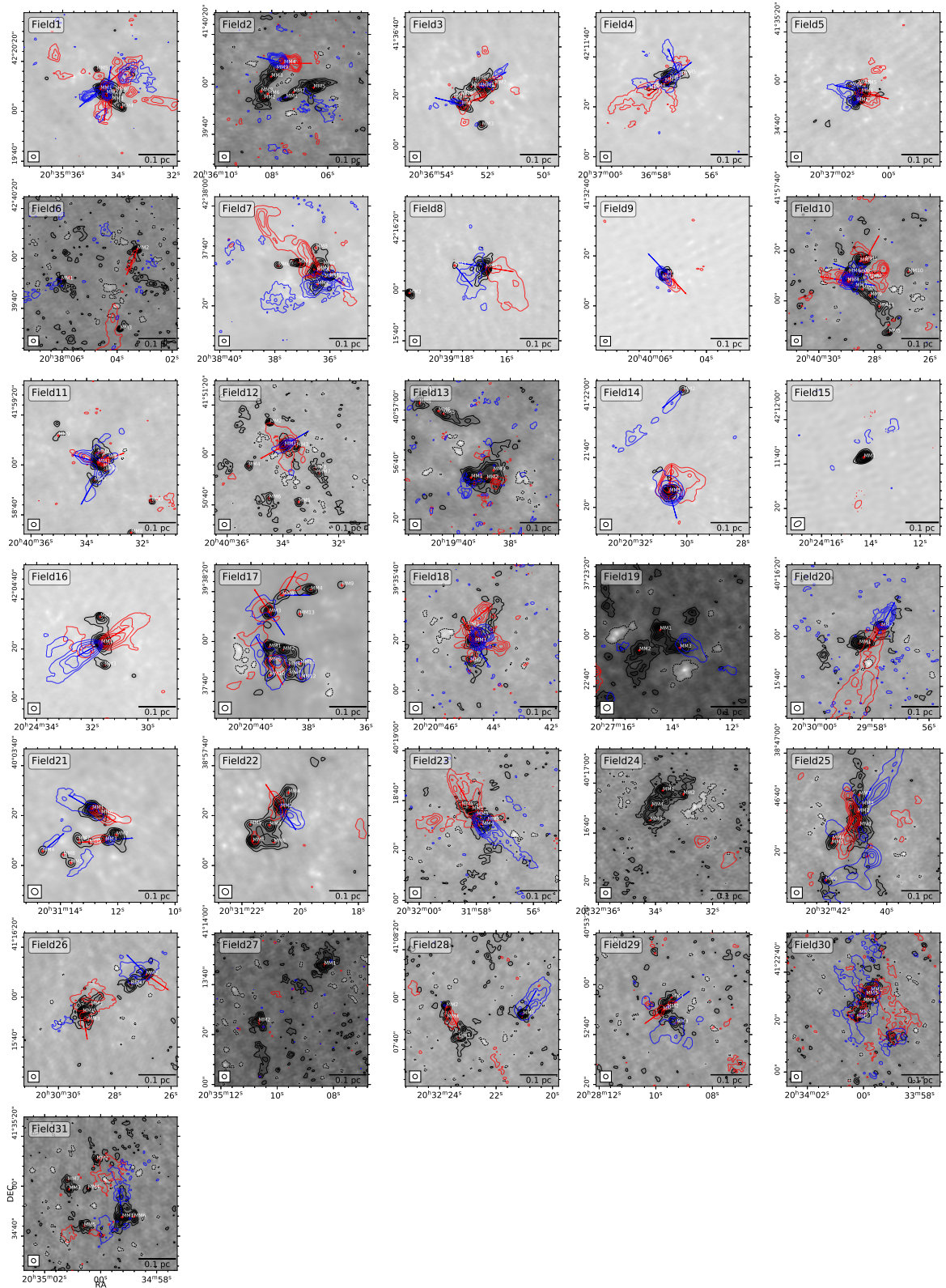


Fig. 2. Molecular outflows detected in CO (2 – 1) in some sources. The blueshifted and redshifted outflows of CO (2 – 1) are plotted in blue and red contours, respectively. The contour levels are $(-3, 3, 6, 9, 12, 15, 18, 24, 36, 48, 60) \times \sigma$, where σ is the rms of the the integrated CO emission. The blue and red arrows mark the outflow axes identified in the region. The grayscale images and black contours show SMA 1.3mm continuum emission. The contour levels are the same as in Fig 1. The extracted dust condensation is marked by a black cross.

flow. Among the 27 dense-gas-traced condensations, only nine display velocity gradients roughly perpendicular to the outflow axis. We label these condensations as disk candidates.

To better illustrate the gas kinematics and investigate whether the velocity gradient is consistent with rotation, we checked the PV cuts in the direction of the velocity gradient (see

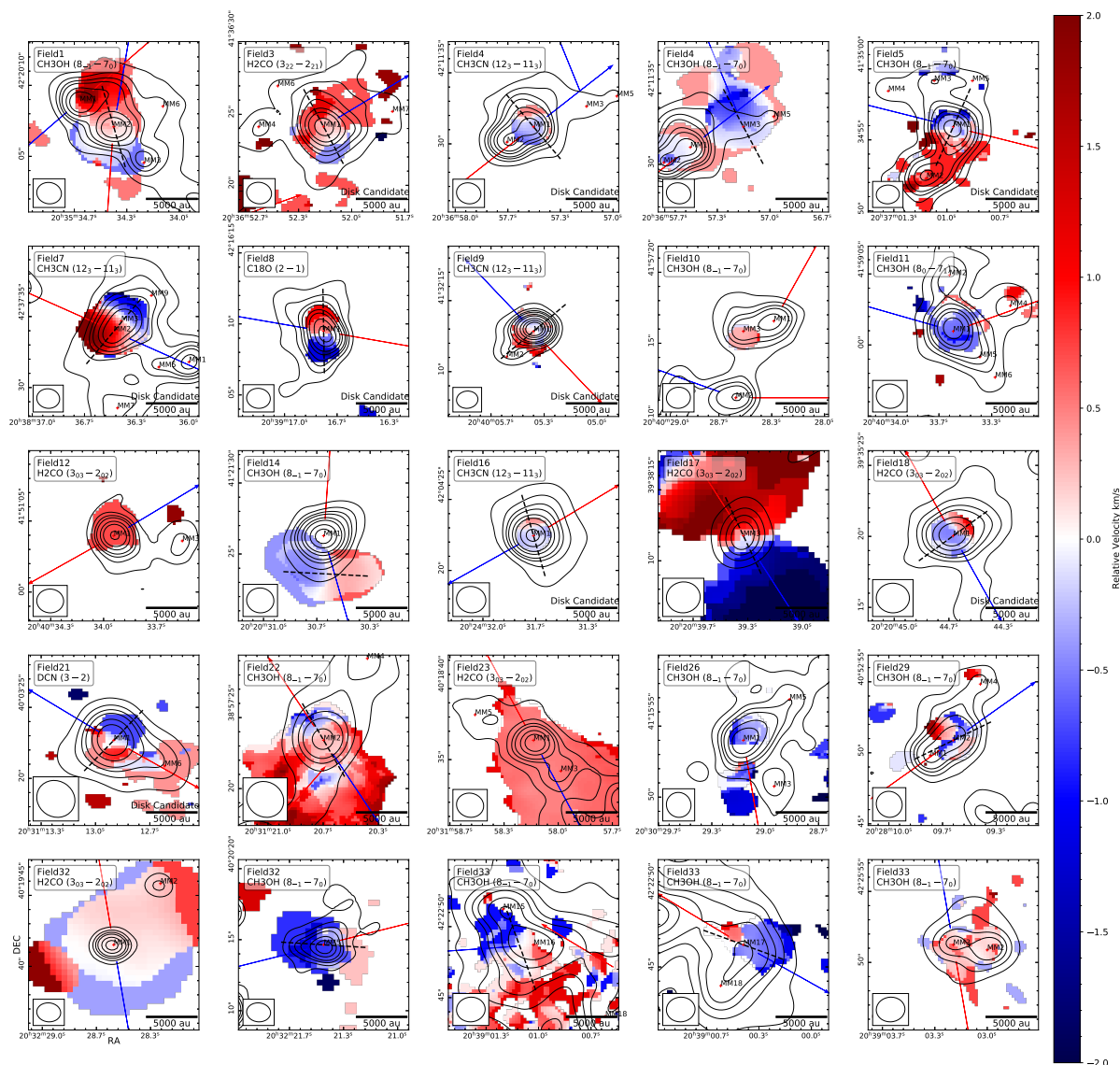


Fig. 3. Intensity-weighted mean velocity maps of representative molecular line emission toward all dense-gas-traced sources, overlaid with the SMA 1.3mm continuum emission contours, the same as in Fig 1. The background color map shows the relative velocity to the systemic velocity of the source. The blue and red arrows represent the blueshifted and redshifted CO outflow axis, respectively. The dashed black lines indicate the velocity gradient orientation inferred from molecular line kinematics. Each panel is labeled with the species name and the excitation energy (in Kelvin) of the upper level of the transition. The label “disk candidate” on the bottom right marks the disk candidates in our sample.

Fig 4). The plots of four identified disk candidates (Field3 MM1, Field8 MM1, Field18 MM1, and Field21 MM1) roughly exhibit a butterfly-shaped feature that is characteristic of Keplerian rotation. We overlaid red Keplerian curves on the PV plots of these four sources. It should be noted that these Keplerian curves are shown only for comparison purposes and are not fitting models. Precise mass estimates of the central protostars from the P-V plots still need higher-resolution observations to resolve the “true disks,” and to constrain the inclination of the disk plane. The rest plots show features that more closely resemble rigid-body rotation than Keplerian rotation. These features are also seen in simulations (e.g., Ahmadi et al. 2019) and observational data (e.g., Cesaroni et al. 2017) with comparable resolutions to our SMA observations. This is likely caused by the insufficient resolution. The contributions of unresolved disks and infalling, rotating envelopes are heavily blended, and thus make the Keplerian curve not fit well with the observational data. Higher-

resolution observations are needed to separate the contributions of the disk and envelope.

4. Discussion

In recent years, many disk candidates around massive protostars have been detected (Beltrán & de Wit 2016). The resolution of these observations is typically on the order of 1000 au or coarser, comparable to our SMA observations. However, it is worth noting that these disk-like structures are more likely infalling, rotating envelopes or “toroids” (Cesaroni et al. 2007; Beltrán & de Wit 2016), rather than true accretion disks on a smaller scale. The true accretion disks should generally have sizes on the order of 100 au, as revealed by recent ALMA observations (e.g., Maud et al. 2018; Ilee et al. 2018; Ginsburg et al. 2018; Jiménez-Serra et al. 2020). Since circumstellar disks are usually believed to mediate material onto protostars from the rotating envelopes,

Table 2. Information on the spectral lines

Line ID	Transition	Frequency GHz	E_{up} K
1	C ¹⁸ O 2 – 1	219.560358	15.8
2	¹³ CO 2 – 1	220.398684	15.9
3	¹² CO 2 – 1	230.538000	16.6
4	SiO 5 – 4	217.104919	31.3
5	DCN 3 – 2	217.238538	20.9
6	SO 6 ₅ – 5 ₄	219.949442	35.0
7	H ₂ CO 3 _{0,3} – 2 _{0,2}	218.222195	21.0
8	H ₂ CO 3 _{2,2} – 2 _{2,1}	218.475632	68.1
9	H ₂ CO 3 _{2,1} – 2 _{2,0}	218.760066	68.1
10	CH ₃ OH 4 _{2,2} – 3 _{1,2} E	218.440050	45.4
11	CH ₃ OH 8 _{0,8} – 7 _{1,6} E	220.078561	96.6
12	CH ₃ OH 8 _{-1,8} – 7 _{0,7} E	229.758756	89.1
13	CH ₃ CN 12 ₀ – 11 ₀	220.747261	68.9
14	CH ₃ CN 12 ₁ – 11 ₁	220.743011	76.0
15	CH ₃ CN 12 ₂ – 11 ₂	220.730260	97.4
16	CH ₃ CN 12 ₃ – 11 ₃	220.709016	133.2
17	CH ₃ CN 12 ₄ – 11 ₄	220.679287	183.2
18	CH ₃ CN 12 ₅ – 11 ₅	220.641084	247.4
19	CH ₃ CN 12 ₆ – 11 ₆	220.594423	325.9
20	CH ₃ CN 12 ₇ – 11 ₇	220.583550	418.6
21	CH ₃ CN 12 ₈ – 11 ₈	220.475807	525.6

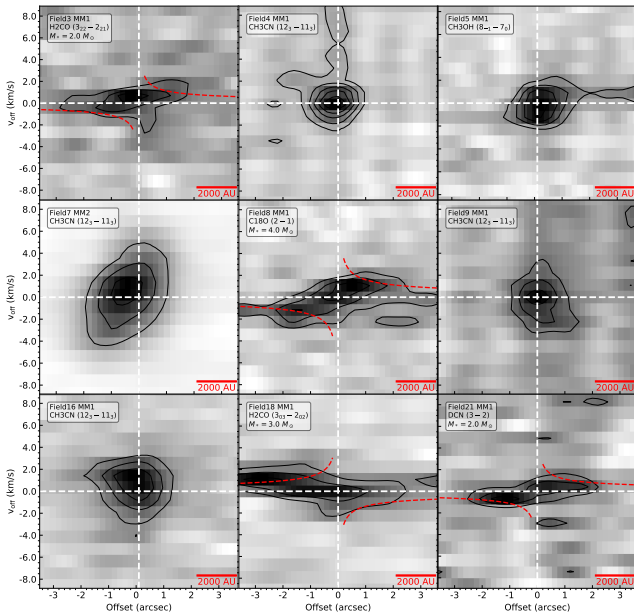


Fig. 4. PV diagram of spectral lines toward the disk candidates, cut along the dashed black lines shown in Fig 3. The dashed red lines show the Keplerian rotation curves for central masses labeled in the upper left. The black contours correspond to 3, 5, 7, 9, 11, and 13 σ levels. The vertical line marks the reference point. The horizontal line indicates the systemic velocity.

the detection of the rotating structures suggests the existence of embedded circumstellar disks.

With high-resolution SMA observations ($\sim 1.8''$), we built up a unique sample consisting of 49 dust condensations associated with molecular outflows. Considering the well-established disk-outflow association in various environments (Cesaroni et al. 2007), we expected to find evidence of a rotating disk or enve-

lope in each outflow-associated condensation. However, only 27 condensations were detected in high-density tracers, and these dense-gas-traced condensations are our targets in searching for rotating evidence. Among the dense-gas-traced condensations, nine condensations show velocity gradients perpendicular to the outflow axis, indicating that these sources may host rotating envelopes or toroids with circumstellar disks embedded in them. The properties of these identified disk candidates are discussed in 4.1. The other dense-gas-traced condensations have no clear velocity gradients or show velocity gradients parallel to the CO outflow axis, which is against the disk hypothesis. The missing rotation signs in these sources are discussed in 4.2. For the rest of the outflow-associated condensations, we do not detect appropriate molecular line emission for studying the kinematics of dense gas around these sources. More sensitive observations are needed to confirm whether these sources are disk candidates.

4.1. Properties of identified disk candidates

Cao et al. (2021) determined the dust temperature of identified dust condensations (refer to their Appendix B) through a combination of two results: the large-scale ($\sim 36''$) dust temperature map from SED fitting results of *Herschel* data and a power law radial temperature profile $T(r) \propto r^{-0.4} L_*^{0.2}$ obtained from an approximate radiative transfer model, where L_* represents the luminosity of the central heating source (protostars). The results are listed in Table 3. It is important to note that since the *Herschel* data cannot resolve the MDCs, the derived dust temperature can be used as a lower limit when a central heating source is lacking. Additionally, CH₃CN and H₂CO lines have been detected in certain sources, and we employed the XCLASS (eXtend CASA Line Analysis Software Suite tool, Möller et al. (2017)) to estimate the molecular gas temperature of these sources. Detailed information on the molecular gas temperature calculation can be found in Appendix B.

For the gas mass estimates, Cao et al. (2021) assumed optically thin dust emission and adopted the equation:

$$M_{\text{gas}} = \frac{g F_{\nu} D^2}{B_{\nu}(T) \kappa_{\nu}}, \quad (1)$$

where M_{gas} is the gas mass of the condensation, g is the gas-to-dust mass ratio, F_{ν} the dust flux density at frequency, ν , D the source distance that is set to 1.4 kpc, $B_{\nu}(T)$ the Planck function at dust temperature, T , and κ_{ν} the dust opacity coefficient. They adopted a gas-to-dust mass ratio of 100 and a dust opacity, $\kappa_{\nu} = 10(\nu/1\text{THz})^{\beta}$ in $\text{cm}^2 \text{g}^{-1}$, following the HOBYS consortium³ (e.g., Tigé et al. 2017). The dust opacity power law index β used here is two. The gas mass of disk candidates ranges from $4M_{\odot}$ to $80M_{\odot}$.

4.2. Why don't all outflow sources show evidence of rotation?

Given that accretion disks are physically connected to outflows, we expected to detect evidence of rotating disks in all outflow-associated condensations. For sources without the emission of dense gas tracers, we cannot determine their kinematics. These sources were excluded from our analyses. So, our analysis focused on the 27 dense-gas-traced condensations. The disk candidate detection rate in the dense-gas-traced group is only $9/27=33.3\%$, and the question is why only one third of outflow sources show evidence of disks.

³ The *Herschel* imaging survey of OB young stellar objects. <http://www.herschel.fr/cea/hobys/en/index.php>

Table 3.

Information on the dust condensations associated with outflow in our SMA observations

Condensation	R.A. (J2000)	Dec (J2000)	T_{dust}^a (K)	M_{gas}^b (M_{\odot})	Size (pc)	$\text{PA}_{\text{grad}}^c$ (deg)	PA_{out}^d (deg)	Molecule ^d Species	Radio ^e Source	Class ^f	Group ^g
Field3 MM1	20:36:52.17	+41:36:24.09	40	6.6	0.016	28	132	DCN/H ₂ CO	UC/HC	Class I*	Disk Candidate
Field4 MM1	20:36:57.67	+42:11:30.18	37	40	0.019	40	127	DCN/H ₂ CO/CH ₃ OH/ CH ₃ CN	Jet/Wind	...	Disk Candidate
Field5 MM1	20:37:00.96	+41:34:55.79	31	6.5	0.016	156	75	DCN/H ₂ CO/CH ₃ OH/ CH ₃ CN	Jet/Wind	Class I*	Disk Candidate
Field7 MM2	20:38:36.49	+42:37:33.79	35	10.9	0.016	140	65	DCN/H ₂ CO/CH ₃ OH/ CH ₃ CN	UC/HC	Class I*	Disk Candidate
Field8 MM1	20:39:16.74	+42:16:09.31	40	9.1	0.015	1	80	C ¹⁸ O/DCN/H ₂ CO	Jet/Wind	FS	Disk Candidate
Field9 MM1	20:40:05.39	+41:32:13.02	17	84.2	0.011	130	43	DCN/H ₂ CO/CH ₃ OH/ CH ₃ CN	Jet/Wind	Class I	Disk Candidate
Field16 MM1	20:24:31.68	+42:04:22.51	32	15.2	0.016	16	120	DCN/H ₂ CO/CH ₃ OH/ CH ₃ CN	Jet/Wind	Class I*	Disk Candidate
Field18 MM1	20:20:44.65	+39:35:20.11	27	3.7	0.021	126	30	DCN/H ₂ CO	Jet/Wind	Class I	Disk Candidate
Field21 MM1	20:31:12.90	+40:03:22.77	34	15.2	0.022	136	60	DCN/H ₂ CO/CH ₃ OH	Jet/Wind	Class I	Disk Candidate
Field1 MM1	20:35:34.62	+42:20:08.95	18	21.4	0.019	...	130	DCN/H ₂ CO/CH ₃ OH	N	...	Dense-Gas-Traced
Field1 MM2	20:35:34.41	+42:20:06.93	25	7.6	0.015	16	175	DCN/H ₂ CO/CH ₃ OH	N	Class I	Dense-Gas-Traced
Field4 MM3	20:36:57.16	+42:11:32.73	18	0.9	0.013	28	22	DCN/H ₂ CO/CH ₃ OH	N	...	Dense-Gas-Traced
Field10 MM3	20:40:28.51	+41:57:15.86	18	3.4	0.015	...	150	CH ₃ OH	N	...	Dense-Gas-Traced
Field11 MM1	20:40:33.57	+41:59:01.07	37	4.2	0.016	...	73	DCN/H ₂ CO/CH ₃ OH	Jet/Wind	Class I	Dense-Gas-Traced
Field12 MM1	20:40:33.93	+41:51:03.99	22	1.9	0.014	...	123	H ₂ CO	Jet/Wind	Class I*	Dense-Gas-Traced
Field14 MM1	20:20:30.63	+41:21:26.27	42	13.1	0.015	87 ^g	175	DCN/H ₂ CO/CH ₃ OH	UC/HC	Class I*	Dense-Gas-Traced
Field17 MM3	20:20:39.36	+39:38:11.76	21	8.5	0.019	25	33	H ₂ CO	Jet/Wind	...	Dense-Gas-Traced
Field22 MM2	20:31:20.67	+38:57:23.46	18	10.3	0.023	30	34	H ₂ CO/CH ₃ OH	Jet/Wind	...	Dense-Gas-Traced
Field23 MM1	20:31:58.15	+40:18:36.19	26	1.3	0.014	...	29	H ₂ CO	Jet/Wind	Class I	Dense-Gas-Traced
Field26 MM1	20:30:29.13	+41:15:53.93	21	10.4	0.019	...	10	H ₂ CO/CH ₃ OH	Jet/Wind	...	Dense-Gas-Traced
Field29 MM2	20:28:09.60	+40:52:51.00	23	2.6	0.019	116	126	H ₂ CO/CH ₃ OH	N	...	Dense-Gas-Traced
Field32 MM1	20:32:28.56	+40:19:41.52	43	1.6	0.010	...	10	H ₂ CO	N	FS	Dense-Gas-Traced
Field32 MM5	20:32:21.46	+40:20:14.51	16	8.3	0.014	87	105	H ₂ CO/CH ₃ OH	Jet/Wind	...	Dense-Gas-Traced
Field33 MM2	20:39:03.00	+42:25:51.04	37	32.0	0.020	...	-160	DCN/H ₂ CO/CH ₃ OH	N	...	Dense-Gas-Traced
Field33 MM3	20:39:03.23	+42:25:51.37	18	20.0	0.019	...	10	DCN/H ₂ CO/CH ₃ OH	N	...	Dense-Gas-Traced
Field33 MM16	20:39:01.03	+42:22:48.72	35	14.0	0.017	...	110	DCN/H ₂ CO/CH ₃ OH	UC/HC	Class I	Dense-Gas-Traced
Field33 MM17	20:39:00.43	+42:22:46.56	27	43.0	0.029	70	60	DCN/H ₂ CO/CH ₃ OH	N	...	Dense-Gas-Traced
Field2 MM4	20:36:07.55	+41:40:08.56	42	0.3	0.017	...	90	...	Jet/Wind	Class I*	Outflow-Associated
Field3 MM2	20:36:52.20	+41:36:08.80	24	5.5	0.015	...	72	...	Jet/Wind	...	Outflow-Associated
Field6 MM2	20:38:03.27	+42:40:03.64	16	1.7	0.014	...	157	...	Jet/Wind	...	Outflow-Associated
Field8 MM3	20:39:17.87	42:16:10.10	17	0.6	0.015	...	40	...	N	...	Outflow-Associated
Field10 MM2	20:40:28.56	+41:57:11.23	23	1.4	0.015	...	80	...	N	Class I	Outflow-Associated
Field10 MM4	20:40:28.96	+41:57:07.90	26	0.8	0.017	...	80	...	N	Class I	Outflow-Associated
Field11 MM3	20:40:33.72	+41:58:53.81	23	1.2	0.015	...	150	...	N	...	Outflow-Associated
Field14 MM2	20:20:30.12	+41:22:07.00	18	4.3	0.017	...	130	...	N	...	Outflow-Associated
Field17 MM4	20:20:37.93	+39:38:20.86	19	10.3	0.020	...	10	...	N	...	Outflow-Associated
Field17 MM5	20:20:39.35	+39:37:52.43	22	7.2	0.026	...	30	...	Jet/Wind	...	Outflow-Associated

(Continued)

Condensation	R.A. (J2000)	Dec (J2000)	T_{dust}^d (K)	M_{gas}^b (M_{\odot})	Size (pc)	PA $_{\text{grad}}^c$ (deg)	PA $_{\text{out}}$ (deg)	Molecule d Species	Radio e Source	Class f	Group g
Field17 MM8	20:20:38.90	+39:38:18.62	42	2.6	0.029	...	120	...	N	Class I	Outflow-Associated
Field18 MM3	20:20:44.89	+39:35:26.39	20	0.5	0.018	...	130	...	N	...	Outflow-Associated
Field20 MM2	20:29:57.67	+40:16:04.22	22	0.9	0.017	...	150	...	N	Class II	Outflow-Associated
Field21 MM3	20:31:12.42	+40:03:10.24	30	1.0	0.020	...	95	...	N	Class I*	Outflow-Associated
Field21 MM4	20:31:14.62	+40:03:05.91	35	1.6	0.023	...	-50	...	N	...	Outflow-Associated
Field21 MM7	20:31:13.37	+40:03:10.39	38	1.5	0.026	...	40	...	Jet/Wind	...	Outflow-Associated
Field22 MM3	20:31:21.05	+38:57:16.04	18	3.1	0.022	...	-30	...	N	...	Outflow-Associated
Field25 MM2	20:32:41.00	+38:46:36.44	15	4.9	0.032	...	150	...	N	...	Outflow-Associated
Field26 MM2	20:30:26.88	+41:16:09.00	21	4.9	0.015	...	45	...	N	...	Outflow-Associated
Field28 MIM1	20:32:21.05	+41:07:54.12	30	2.2	0.014	...	150	...	Jet/Wind	Class I	Outflow-Associated
Field28 MIM2	20:32:23.76	+41:07:57.23	28	1.4	0.015	...	30	...	N	Class I	Outflow-Associated
Field31 MIM1	20:34:59.24	+41:34:47.50	21	2.8	0.023	...	8	...	N	...	Outflow-Associated

Notes.

^(a) Dust temperature estimated by Cao et al. (2021). The $1-\sigma$ uncertainty of T is $\sigma_T = 4$ K.

^(b) Gas mass estimated by Cao et al. (2021). Monte-Carlo simulations show that the $1-\sigma$ uncertainty of M_{gas} is ~ 0.26 dex ($\sim 64\%$).

^(c) Orientation of the velocity gradient revealed by the selected line emission.

^(d) Detection of dense gas tracers, CH_3CN , CH_3OH , and H_2CO , in each dust condensation associated with outflow. Information on the transitions of these molecules is listed in Table 2. "..." means no dense gas tracers were detected as showing the kinematics. " C^{18}O " means the C^{18}O ($2-1$) emission in Field8 MM1 also traces dense gas surrounding the condensation and reveals the evidence of a rotating structure.

^(e) Radio sources identified by Wang et al. (2022). "UC/HC" means the radio detection is likely from the ultra- or hyper-compact H II region. "Jet/Wind" means the radio detection is likely from a radio jet or wind. "N" means no radio source coincides with the condensation.

^(f) IR Classification identified by Kryukova et al. (2014). "Class" implies the mid-infrared color of these condensations, which can in turn indicate the YSO evolutionary stage of these condensations. "FS" means a "flat spectrum" that has a spectral index, α , ranging from -0.3 to 0.3 . The discussions of the mid-infrared colors are shown in Section 4.2.2

^(g) Classifications of the condensations. "Outflow-associated" means these condensations are associated with outflow. "Dense-gas-traced" are condensations included in "outflow-associated" condensations that have emission of dense gas tracers. "Disk candidate" condensations are included in dense-gas-traced condensations showing evidence of a rotating disk. The classifications of the condensations are described in Section 3.2.

^(h) The clear velocity gradient from line emission away from a potential outflow central source. So, it is not identified as a disk candidate.

⁽ⁱ⁾ The sources are saturated or unresolved in a $24 \mu\text{m}$ image, which means photometry is unavailable.

4.2.1. Non-detection of rotating structures

There are several explanations for the lack of a velocity gradient toward some dense-gas-traced condensations. First, in contrast to the simplified classic paradigm of a stable disk-jet system, many simulations (Myers et al. 2013; Seifried et al. 2015; Rosen et al. 2016) predict that protostellar cores may accrete material through asymmetrical filaments without a large, stable Keplerian disk, and some recent ALMA observations support this scenario (e.g., Goddi et al. 2020). However, it needs higher-spatial-resolution observations to confirm whether these sources without rotating structures in our sample actually accrete material through filamentary flows. Second, several condensations, for example Field4 MM3 and Field10 MM3, are located in complex regions. The emission from adjacent energetic events (e.g., accretion flow or jets and outflows) may confuse the velocity field around these condensations and make it difficult to distinguish the rotating structures or toroids. On the other hand, relatively isolated sources, forming in an environment away from other energetic events, have a higher chance of showing detectable rotating structures (e.g., Field9 MM1, Field16 MM1 in this work and G17.64+0.16 in Maud et al. 2018).

The inclination of the disk plane with respect to the line of sight may also affect the observational evidence of a rotating disk. We made a simple simulation following Zhang et al. (2019) to investigate the influence of inclination on disk identification.

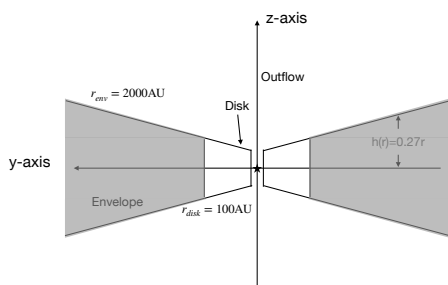


Fig. 5. Schematic diagram of our envelope-disk model. The outflow axis is aligned with the z axis. The inner part of the Keplerian disk starts from the inner boundary, $r_{in} = 10$ au, and extends to the centrifugal barrier, $r_{CB} = 100$ au. The outer envelope ranges from the centrifugal barrier, r_{CB} , to the outer boundary, $r_{out} = 2000$ au.

Fig 5 shows the schematic view of an inner Keplerian-rotating disk embedded in a larger-scale infalling and rotating envelope. The masses of the central protostar, accretion disk, and envelope are $10M_{\odot}$, $3M_{\odot}$, and $5M_{\odot}$, respectively. We assumed an opening angle of 150° for the outflow cavity. The flattened envelope has a radial free-fall velocity. Its rotation velocity can be described as $v_{\phi} \propto r^{-1}$. The inner disk is assumed to be in Keplerian rotation ($v_{rot} \propto r^{-1/2}$). We used open-source software, *RADMC-3D* (Dullemond et al. 2012), and the CASA simulator task *simobserve* to generate synthetic SMA observations for the model with different inclination angles. The settings for the synthetic observation are the same as for our SMA observations, with an angular resolution of $\sim 1.8''$ and a velocity resolution of 1 km s^{-1} . Fig 6 shows the first-moment map of $\text{CH}_3\text{CN} (12_3 - 11_3)$ for the synthetic observation. The simulation indicates that only when the rotation axis is extremely inclined to the line of sight ($\text{incl} \leq 10^{\circ}$) can the velocity structure

of the disk and envelope not be revealed by our SMA observation, meaning the effect of the inclination angles is not the prominent cause of the non-detection of a rotating structure. However, it is worth noting that the orientation of the velocity gradient slightly changes with the inclination. When the disk plane is nearly edge-on ($\text{incl} \geq 80^{\circ}$), the velocity gradient is almost perpendicular to the outflow axis. As the inclination angle decreases, the orientation of the velocity gradient slightly shifts toward the outflow axis. This phenomena is also seen in other simulations (e.g., Ahmadi et al. 2019). We speculate that it may be because the envelope and disk contributions are strongly blended under poor resolutions. The velocity gradients seen at a low inclination angle (including $\leq 30^{\circ}$) are mainly contributed by the infalling-rotating envelope since the line-of-sight velocity component in the disk is very small. The disk contributions become increasingly important as the structures get more inclined. Detailed kinematic analyses using high-resolution simulations and more sophisticated models are necessary to investigate the direction of the velocity gradient changes with the inclination and to what extent this could affect the detection of a rotating disk, which is beyond the scope of this work.

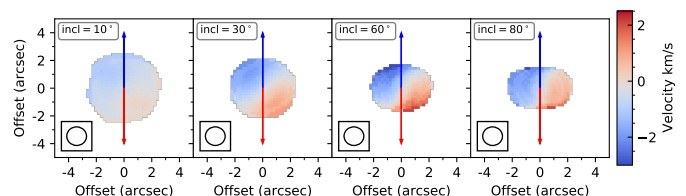


Fig. 6. Synthetic SMA observations made with the CASA task “simobserve” from the outputs of radiative transfer calculations of the envelope-disk model shown in Fig 5. From left to right, the inclination angle of the rotation axis with respect to the line of sight changes from 10° to 80° . The color scale shows the $\text{CH}_3\text{CN} (12_3 - 11_3)$ first-moment map. The red and blue arrows represent redshifted and blueshifted outflows, respectively. The bottom left of each panel shows the synthesized beam.

4.2.2. Comparisons between disk candidates and others

Except for the examples mentioned above, we compared the properties of disk candidates and non-disk dense-gas-traced condensations to further explore the detectability of rotating structures around protostars.

Table 3 lists the parameters of the condensations. To better illustrate the temperature difference between disk and non-disk groups, Fig 7 shows the distribution of dust temperatures for all dense-gas-traced condensations. Most disk candidates, except for Field9 MM1 and Field18 MM1, have dust temperatures exceeding 30 K, with a median temperature of 34 K. On the other hand, the non-disk dense-gas-traced condensations generally have lower dust temperatures, with a median value of 22.5 K. The $1-\sigma$ uncertainty of the dust temperature is $\sigma_T = 4$ K. The difference between the median temperature of disk candidate and non-disk dense-gas-traced sources is about three times the temperature uncertainty. We ran a Kolmogorov-Smirnov test (K-S test) to investigate how significant the temperature difference is between the disk candidate and non-disk dense-gas-traced sources. A p value of ≈ 0.01 was obtained for testing the null hypothesis that the two distributions are identical, indicating a statistically significant difference in dust temperature between the two groups. Even though the dust temperature is derived from the *Herschel* data with a coarser resolution, con-

sidering that the temperatures were uniformly derived for all the sources in our sample, we took it into account in checking the evolutionary stages of the sources. The increasing trend in the dust temperature from disk candidates to non-disk dense-gas-traced condensations suggests disk candidates are more evolved.

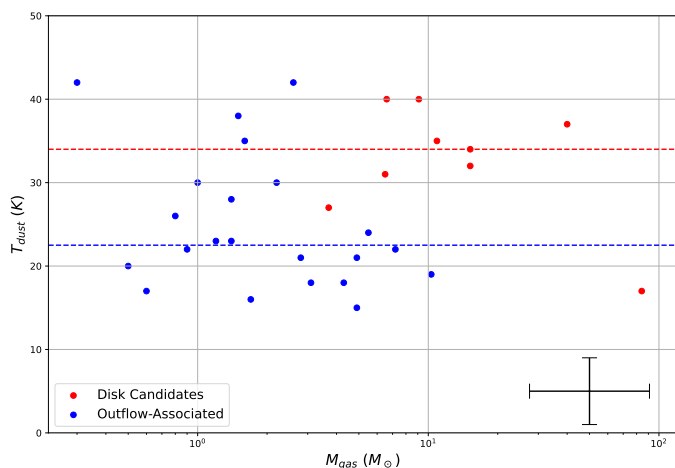


Fig. 7. Dust temperature distribution of all dense-gas-traced condensations in relation of gas mass. Red and blue dots represent disk candidates and non-disk dense-gas-traced condensations, respectively. The dashed red line shows the median temperature of the disk candidates, 34 K. The dashed black line shows the median temperature of the non-disk dense-gas-traced condensations, 22.5 K. In the lower right corner, the vertical and horizontal black error bar indicates the uncertainties of the dust temperature ($\sigma_T = 4$ K) and the gas mass (~ 0.26 dex) from Cao et al. (2021), respectively.

The brightness of radio continuum emission can also to some extent probe the evolution of high-mass star formation. Wang et al. (2022) has made a systematic study of the radio properties of the condensations in our sample with high-angular-resolution VLA observations. They find that the detection rate of radio sources, either in the form of radio jets or wind, or UC/HC HII, increases as the protostellar object evolves. This trend is consistent with that in Rosero et al. (2016). It may come from this that, at a very early stage, the star formation activities are not strong enough to produce detectable radio emission. For example, Tanaka et al. (2016) modeled the evolution of a massive protostar and its associated jet as it is being photoionized by the protostar. In this outflow-confined HII region model, at a very early stage, the ionizing photon luminosity is too low to ionize the outflow, and thus does not produce free-free emission. As a result, the sources without detectable radio emission are more likely at an earlier stage than the sources with radio emission. We cross-checked 49 outflow-associated condensations with their identified radio sources and found that the radio detection rate of disk candidates is 100%, substantially higher than the detection rate of non-disk dense-gas-traced sources, which stands at 9/18=50%. Consequently, disk candidates are generally more evolved than non-disk dense-gas-traced sources, which is consistent with the speculation from the above comparison of dust temperatures.

To further check the evolutionary stages of the sources, we conducted a cross-correlation analysis between the 49 outflow-associated condensations and the mid-infrared sources from the Cygnus-X Archive catalog⁴. By applying a spatial constraint of 2'', approximately the mean size of the condensation, we

found that 23 condensations coincide with *Spitzer* sources (see Table 4). In a previous study, Kryukova et al. (2014) systematically surveyed protostars in the Cygnus-X region using *Spitzer* IRAC and 24 μm photometry. They estimated the spectral index, $\alpha = \delta \log(\lambda F_\lambda) / \delta \log(\lambda)$ in wavelength ranges from 3.6 μm to 24 μm . Based on their estimated spectral index, α , these sources are identified as Class 0/I ($\alpha > 0.3$), flat spectrum ($-0.3 < \alpha < 0.3$), and Class II (using criteria of Gutermuth et al. 2009) young stellar objects (YSOs). We note that Kryukova et al. (2014) classified these protostar candidates only depending on their mid-infrared color, without considering their masses. Therefore, it is important to clarify that a condensation classified as Class 0/I/II or flat spectrum only reflects its IR color and does not mean that it is a low-mass protostar or young star. We used this information to constrain the evolutionary stages of these sources. Apparently, a source dark all the way from 3.6 μm to 24 μm is cold and at an earlier evolutionary stage compared to a source that is detected in several *Spitzer* bands and that could be classified as Class 0/I/II or flat spectrum by Kryukova et al. (2014). Some of the brightest sources in our sample are saturated (e.g., Field7 MM2) or unresolved (e.g., Field2 MM2) at 24 μm , and thus it is not possible to do 24 μm photometry. Kryukova et al. (2014) excluded these sources in their classification catalog, while we notice that these sources always have bright emission at 3.6 μm to 8.0 μm . Therefore, it is reasonable to assume that the sources that are saturated or unresolved at 24 μm are also relatively more evolved. Eventually, we found that more than half of the non-disk (11/18=61.1%) dense-gas-traced condensations are dark in 3.6 μm to 24 μm , while 8/9=88.9% of the disk candidates have bright emission in 3.6 μm to 24 μm . This again suggests that disk candidates are relatively more evolved than non-disk dense-gas-traced sources.

Several studies (e.g., Arce & Sargent 2006; Qiu et al. 2019; Vazzano et al. 2021; Heimsoth et al. 2022) have found that the outflow opening angles increase as the outflow central sources evolve. Within our sample, we notice that the outflows emanating from disk candidates tend to have wide-angle morphology (e.g., Field8 MM1) or irregular shapes (e.g., the blueshifted lobe associated with Field7 MM2), while the outflows originating in non-disk sources always appear to be collimated (e.g., Field1 MM1). This provides another piece of evidence that disk candidates are generally more evolved.

From all the perspectives discussed above, dust condensations with rotating disks or toroids are generally more evolved than other sources. The apparent lack of rotating structures at relatively early evolutionary stages might be due to the outflow-envelope interactions proposed by Arce & Sargent (2006). Table 3 shows that some non-disk dense-gas-traced condensations display velocity gradients roughly parallel to the axis of outflow (e.g., Field1 MM2). For those dense-gas-traced condensations without a clear velocity gradient, their dense gas emission always appear to be elongated along the outflow axis. Since the spatial resolution of our SMA observations is insufficient to resolve the true accretion disk (on the order of 10^2 au) that is embedded within the envelope, the high-density tracers mainly come from the contribution of the high-density envelope (on the order of 10^3 au). In young, deeply embedded sources, the powerful outflow entrains and pushes gas into the envelope, causing the elongated distribution of the dense gas along the outflow axis. As the protostar evolves, the outflow cavities tend to widen. Most of the remaining circumstellar gas is concentrated in the flattened envelope perpendicular to the outflow axis, which is consistent with the model from Zhang et al. (2019). At this stage, it is more common to detect rotating structures or toroids with dense gas tracers.

⁴ <https://irsa.ipac.caltech.edu/cgi-bin/Gator/nph-dd>

Table 4. Infrared properties of outflow-associated condensations

Condensation	R.A. (deg)	Dec (deg)	3.6 μm (mag)	4.5 μm (mag)	5.8 μm (mag)	8.0 μm (mag)	24 μm (mag)	Class ^a
Field1 MM2	308.893524	42.335224	11.00 ± 0.03	8.16 ± 0.02	6.81 ± 0.02	6.09 ± 0.03	1.55 ± 0.07	Class I
Field2 MM4	309.031372	41.669178	5.23 ± 0.02	4.29 ± 0.02	3.16 ± 0.02	2.66 ± 0.02	...*	...
Field3 MM1	309.217438	41.606693	7.37 ± 0.02	5.46 ± 0.02	4.016 ± 0.02	2.677 ± 0.02	...*	...
Field5 MM1	309.253937	41.582123	8.92 ± 0.03	6.69 ± 0.02	5.13 ± 0.02	4.19 ± 0.05	...*	...
Field7 MM2	309.652039	42.625977	...	6.24 ± 0.03	4.55 ± 0.04	3.55 ± 0.04	...*	...
Field8 MM1	309.819672	42.269257	6.49 ± 0.02	5.17 ± 0.02	4.00 ± 0.02	3.24 ± 0.02	0.255 ± 0.02	FS
Field9 MM1	310.02247	41.53695	...	12.07 ± 0.07	11.36 ± 0.11	11.35 ± 0.19	3.02 ± 0.02	Class I
Field10 MM2	310.11898	41.95312	10.83 ± 0.03	9.01 ± 0.03	8.27 ± 0.03	7.95 ± 0.02	1.04 ± 0.02	Class I
Field10 MM4	310.120758	41.952198	8.79 ± 0.02	7.38 ± 0.02	6.37 ± 0.02	5.44 ± 0.02	1.19 ± 0.03	Class I
Field11 MM1	310.139526	41.983509	14.38 ± 0.05	11.52 ± 0.02	11.68 ± 0.08	...	3.91 ± 0.1	Class I
Field12 MM1	310.141357	41.851223	10.28 ± 0.02	8.71 ± 0.02	7.32 ± 0.02	6.32 ± 0.03	...*	...
Field14 MM1	305.127655	41.357201	5.16 ± 0.02	4.34 ± 0.02	2.20 ± 0.02	...*	...*	...
Field16 MM1	306.132111	42.072918	10.80 ± 0.03	7.29 ± 0.02	5.24 ± 0.02	3.97 ± 0.01	...*	...
Field17 MM8	305.162201	39.638287	12.07 ± 0.12	10.08 ± 0.04	8.43 ± 0.04	7.03 ± 0.04	1.43 ± 0.08	Class I
Field18 MM1	305.185699	39.589119	9.09 ± 0.02	7.80 ± 0.02	6.82 ± 0.04	5.87 ± 0.06	2.02 ± 0.1	Class I
Field20 MM2	307.490326	40.267841	8.45 ± 0.02	7.61 ± 0.02	6.99 ± 0.02	6.26 ± 0.02	3.39 ± 0.04	Class II
Field21 MM1	307.803802	40.056416	8.48 ± 0.08	1.343 ± 0.07	Class I
Field21 MM3	307.801636	40.052952	10.76 ± 0.04	9.03 ± 0.02	7.18 ± 0.04	5.80 ± 0.08	...*	...
Field23 MM1	307.99231	40.310028	13.98 ± 0.03	12.19 ± 0.03	11.35 ± 0.04	10.97 ± 0.11	3.68 ± 0.04	Class I
Field28 MM1	308.087738	41.131798	11.12 ± 0.02	8.53 ± 0.02	6.48 ± 0.02	5.07 ± 0.02	0.87 ± 0.02	Class I
Field28 MM2	308.098999	41.132629	13.63 ± 0.04	10.82 ± 0.02	9.03 ± 0.02	8.01 ± 0.04	4.83 ± 0.1	Class I
Field32 MM1	308.119202	40.328213	7.37 ± 0.02	6.30 ± 0.02	5.35 ± 0.02	4.43 ± 0.02	0.98 ± 0.02	FS
Field33 MM16	309.754211	42.380585	11.10 ± 0.04	10.10 ± 0.05	7.48 ± 0.04	5.67 ± 0.05	-0.24 ± 0.03	Class I

Notes.

Infrared properties from Cygnus-X Archive catalog.

^(a) Classification results from Kryukova et al. (2014). “FS” means flat spectrum. “...” means that these IR sources were not selected by Kryukova et al. (2014) since the 24 μm photometry is unavailable for these sources.

^(*) “*” means the emission is saturated or unresolved in this band.

5. Summary

We have shown the results of SMA observations of continuum and molecular line emission toward 31 single-pointing fields and two mosaic fields, covering 48 MDCs in Cygnus-X. The high-resolution observations resolve these MDCs into about 200 dust condensations with sizes of order 0.01 pc, 49 of which are found to be associated with CO outflows. The velocity fields for 27 of these outflow-associated condensations are revealed by high-density tracers (e.g., CH_3CN and CH_3OH lines). Eventually, nine dust condensations are recognized to be rotating, as is evidenced by them showing a velocity gradient perpendicular to the outflow axis. The detected rotating condensations are more likely “toroids” or envelopes with radii on the order of 1000 au, enclosing smaller disks. Further investigations of the P-V diagrams along the velocity gradient reveal cases with butterfly-shaped patterns, indicative of Keplerian-like rotation.

We generated synthetic SMA observations of a disk-envelope model at varying inclination angles with *RADMC-3D*. Even though the model is simplified, the simulation suggests that inclination can hinder the detection of rotating envelopes or toroids only when the rotation axis is largely inclined to the line of sight.

By comparing disk candidates and non-disk dense-gas-traced condensations, we conclude that the disk candidate detection rate could be sensitive to protostellar evolution. In young, deeply embedded sources, the powerful outflows may dominate the kinematics of the envelopes. As the protostar evolves, the outflows carve a wide-angle cavity, resulting in a flattened rotating envelope that is easier to detect. The insufficient angular resolution of our SMA observations makes it difficult to reveal

the deeply embedded “true disk” that has a small size. Observations with a higher resolution and sensitivity are required to figure out whether these disk candidates actually host small-scale Keplerian-like disks and the reason why other dense-gas-traced and outflow-associated condensations do not show evidence of rotating structures.

Acknowledgements. This work is supported by National Key R&D Program of China No. 2022YFA1603100, No. 2017YFA0402604, the National Natural Science Foundation of China (NSFC) grant U1731237, and the science research grant from the China Manned Space Project with No. CMS-CSST-2021-B06.

References

- Ahmadi, A., Beuther, H., Mottram, J. C., et al. 2018, *A&A*, 618, A46
 Ahmadi, A., Kuiper, R., & Beuther, H. 2019, *A&A*, 632, A50
 Andrews, S. M., Huang, J., Pérez, L. M., et al. 2018, *ApJ*, 869, L41
 Ansdell, M., Williams, J. P., Trapman, L., et al. 2018, *ApJ*, 859, 21
 Ansdell, M., Williams, J. P., van der Marel, N., et al. 2016, *ApJ*, 828, 46
 Arce, H. G. & Sargent, A. I. 2006, *ApJ*, 646, 1070
 Beltrán, M. T. & de Wit, W. J. 2016, *A&A Rev.*, 24, 6
 Beltrán, M. T., Sánchez-Monge, Á., Cesaroni, R., et al. 2014, *A&A*, 571, A52
 Beuther, H., Mottram, J. C., Ahmadi, A., et al. 2018, *A&A*, 617, A100
 Bontemps, S., Motte, F., Csengeri, T., & Schneider, N. 2010, *A&A*, 524, A18
 Briggs, D. S. 1995, in *American Astronomical Society Meeting Abstracts*, Vol. 187, American Astronomical Society Meeting Abstracts, 112.02
 Cao, Y., Qiu, K., Zhang, Q., et al. 2019, *ApJS*, 241, 1
 Cao, Y., Qiu, K., Zhang, Q., Wang, Y., & Xiao, Y. 2021, *ApJ*, 918, L4
 Cesaroni, R., Galli, D., Lodato, G., Walmsley, C. M., & Zhang, Q. 2007, in *Protostars and Planets V*, ed. B. Reipurth, D. Jewitt, & K. Keil, 197
 Cesaroni, R., Galli, D., Neri, R., & Walmsley, C. M. 2014, *A&A*, 566, A73
 Cesaroni, R., Sánchez-Monge, Á., Beltrán, M. T., et al. 2017, *A&A*, 602, A59
 Cheng, Y., Tobin, J. J., Yang, Y.-L., et al. 2022, *ApJ*, 933, 178
 Dullemond, C. P., Juhasz, A., Pohl, A., et al. 2012, *RADMC-3D: A multi-purpose radiative transfer tool*, *Astrophysics Source Code Library*, record ascl:1202.015

- Ginsburg, A., Bally, J., Goddi, C., Plambeck, R., & Wright, M. 2018, *ApJ*, 860, 119
- Ginsburg, A., Goddi, C., Kruijssen, J. M. D., et al. 2017, *ApJ*, 842, 92
- Girart, J. M., Estalella, R., Fernández-López, M., et al. 2017, *ApJ*, 847, 58
- Goddi, C., Ginsburg, A., Maud, L. T., Zhang, Q., & Zapata, L. A. 2020, *ApJ*, 905, 25
- Gutermuth, R. A., Megeath, S. T., Myers, P. C., et al. 2009, *ApJS*, 184, 18
- Harries, T. J., Douglas, T. A., & Ali, A. 2017, *MNRAS*, 471, 4111
- Heimsoth, D. J., Stephens, I. W., Arce, H. G., et al. 2022, *ApJ*, 927, 88
- Ilee, J. D., Cyganowski, C. J., Brogan, C. L., et al. 2018, *ApJ*, 869, L24
- Jiménez-Serra, I., Báez-Rubio, A., Martín-Pintado, J., Zhang, Q., & Rivilla, V. M. 2020, *ApJ*, 897, L33
- Kahn, F. D. 1974, *A&A*, 37, 149
- Klassen, M., Pudritz, R. E., Kuiper, R., Peters, T., & Banerjee, R. 2016, *ApJ*, 823, 28
- Kryukova, E., Megeath, S. T., Hora, J. L., et al. 2014, *AJ*, 148, 11
- Maud, L. T., Cesaroni, R., Kumar, M. S. N., et al. 2018, *A&A*, 620, A31
- McMullin, J. P., Waters, B., Schiebel, D., Young, W., & Golap, K. 2007, in *Astronomical Society of the Pacific Conference Series*, Vol. 376, *Astronomical Data Analysis Software and Systems XVI*, ed. R. A. Shaw, F. Hill, & D. J. Bell, 127
- Men'shchikov, A., André, P., Didelon, P., et al. 2012, *A&A*, 542, A81
- Meyer, D. M. A., Kuiper, R., Kley, W., Johnston, K. G., & Vorobyov, E. 2018, *MNRAS*, 473, 3615
- Möller, T., Endres, C., & Schilke, P. 2017, *A&A*, 598, A7
- Motte, F., Bontemps, S., Schilke, P., et al. 2007, *A&A*, 476, 1243
- Myers, A. T., McKee, C. F., Cunningham, A. J., Klein, R. I., & Krumholz, M. R. 2013, *ApJ*, 766, 97
- Qiu, K., Wyrowski, F., Menten, K., Zhang, Q., & Güsten, R. 2019, *ApJ*, 871, 141
- Rosen, A. L., Krumholz, M. R., McKee, C. F., & Klein, R. I. 2016, *MNRAS*, 463, 2553
- Rosero, V., Hofner, P., Claussen, M., et al. 2016, *ApJS*, 227, 25
- Sánchez-Monge, Á., Cesaroni, R., Beltrán, M. T., et al. 2013, *A&A*, 552, L10
- Schneider, N., Bontemps, S., Simon, R., et al. 2006, *A&A*, 458, 855
- Seifried, D., Banerjee, R., Pudritz, R. E., & Klessen, R. S. 2015, *MNRAS*, 446, 2776
- Tanaka, K. E. I., Tan, J. C., & Zhang, Y. 2016, *ApJ*, 818, 52
- Tigé, J., Motte, F., Russeil, D., et al. 2017, *A&A*, 602, A77
- Tobin, J. J., Sheehan, P. D., Reynolds, N., et al. 2020, *ApJ*, 905, 162
- Tripathi, A., Andrews, S. M., Birnstiel, T., & Wilner, D. J. 2017, *ApJ*, 845, 44
- Uyaniker, B., Fürst, E., Reich, W., Aschenbach, B., & Wielebinski, R. 2001, *A&A*, 371, 675
- Vazzano, M. M., Fernández-López, M., Plunkett, A., et al. 2021, *A&A*, 648, A41
- Wang, K. S., van der Tak, F. F. S., & Hogerheijde, M. R. 2012, *A&A*, 543, A22
- Wang, Y., Qiu, K., Cao, Y., et al. 2022, *ApJ*, 927, 185
- Wendker, H. J., Higgs, L. A., & Landecker, T. L. 1991, *A&A*, 241, 551
- Wolfire, M. G. & Cassinelli, J. P. 1987, *ApJ*, 319, 850
- Yang, K., Qiu, K., & Pan, X. 2023, *A&A* submitted
- Zhang, Q., Hunter, T. R., & Sridharan, T. K. 1998, *ApJ*, 505, L151
- Zhang, X., Qiu, K., Zhang, Q., et al. 2023, *A&A* submitted
- Zhang, Y., Tan, J. C., Sakai, N., et al. 2019, *ApJ*, 873, 73

Appendix A: Dust continuum and CO outflow maps

Table A.1. Physical parameters of the MDCs

Field	Motte07 ^b	MDC ^c	R.A. (J2000)	Decl. (J2000)
1	N02/N03	220	20:35:34.630	+42:20:08.787
2	N05/N06	274	20:36:07.300	+41:39:57.994
3	N10	725	20:36:52.199	+41:36:22.991
4	N12/N13	248	20:36:57.397	+42:11:27.997
5	N14	714	20:37:00.900	+41:34:57.002
6	N22/N24	1267	20:38:04.599	+42:39:53.997
7	N30/N31/N32	1112/1231	20:38:37.401	+42:37:32.994
8	N56	698/1179	20:39:16.897	+42:16:07.003
9	N63	341	20:40:05.202	+41:32:13.003
10	N64/N65	801	20:40:28.397	+41:57:10.997
11	N68	684	20:40:33.499	+41:59:02.995
12	N69	4315/4797	20:40:33.698	+41:50:59.000
13	NW01/NW02	327/742	20:19:38.998	+40:56:45.006
14	NW04/NW05/NW07	640/675	20:20:30.503	+41:21:39.998
15	NW12	839	20:24:14.301	+42:11:43.001
16	NW14	310	20:24:31.701	+42:04:22.999
17	S06/S07/S08/S09	507/753	20:20:38.599	+39:38:00.006
18	S10	798	20:20:44.400	+39:25:19.999
19	S15	874	20:27:13.996	+37:22:57.997
20	S29	723	20:29:58.297	+40:15:57.994
21	S30/S31	509	20:31:12.599	+40:03:15.996
22	S32	351	20:31:20.303	+38:57:16.002
23	S34	1225	20:31:57.801	+40:18:30.004
24	S41	892	20:32:33.397	+40:16:42.997
25	S42/S43	540	20:32:40.799	+38:46:30.994
26	...	214/247	20:30:28.503	+41:15:55.000
27	...	302/520	20:35:09.499	+41:13:29.995
28	...	340	20:32:22.500	+41:07:55.996
29	...	370	20:28:09.402	+40:52:49.995
30	...	608	20:34:00.003	+41:22:25.001
31	...	1460/2320	20:35:00.002	+41:34:57.002
32 ^a	S36/S37	1454	20:32:21.850	+40:20:00.708
	S38	2210	20:32:22.302	+40:19:19.524
33 ^a	N36/N40/N41	1018	20:38:59.333	+42:23:37.183
	N37/N43	5417	20:38:58.299	+42:24:35.896
	N38/N48	699	20:39:00.023	+42:22:16.036
	N44	1467	20:38:59.642	+42:23:06.864
	N51	1243	20:39:02.409	+42:25:09.124
	N52/N53	1599	20:39:03.131	+42:26:00.013

Notes.

^(a) Mosaic field

^(b) MDCs from Motte et al. (2007)

^(c) MDCs from Cao et al. (2021) covered in our SMA field

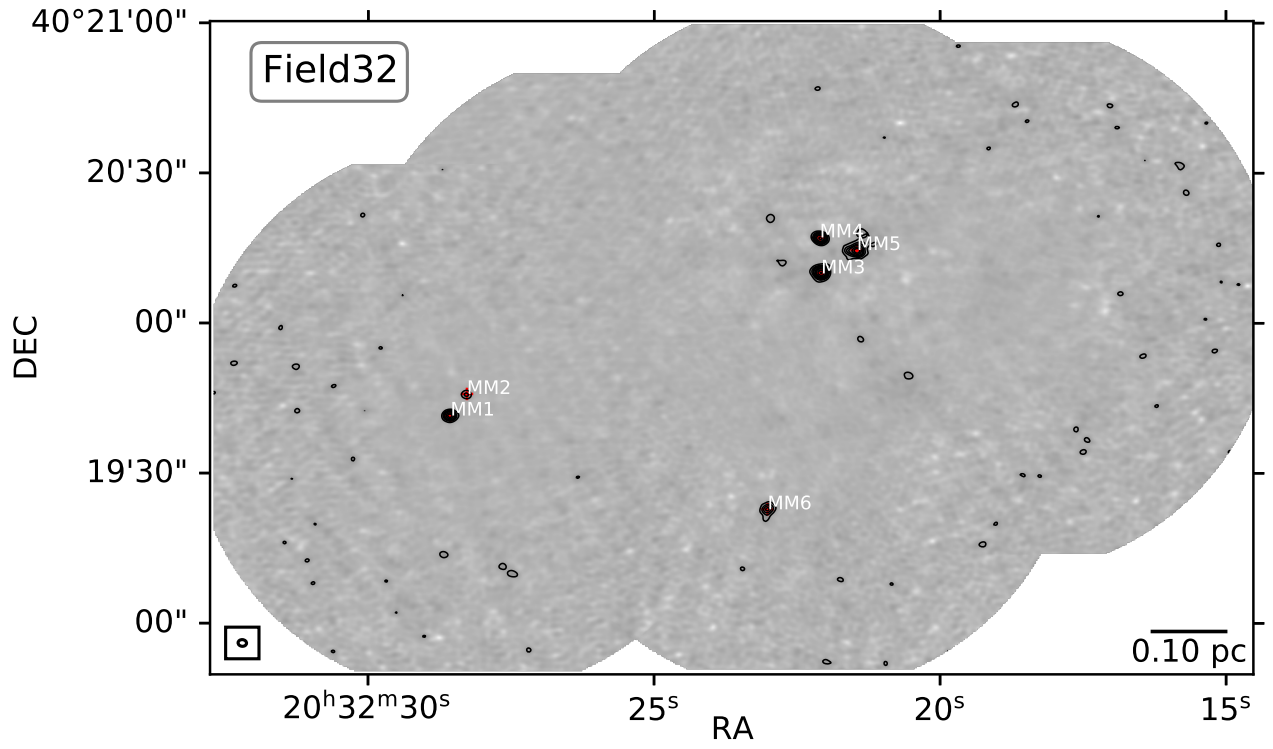


Fig. A.1. SMA 1.3 mm continuum map of DR15. Similar to Fig 1

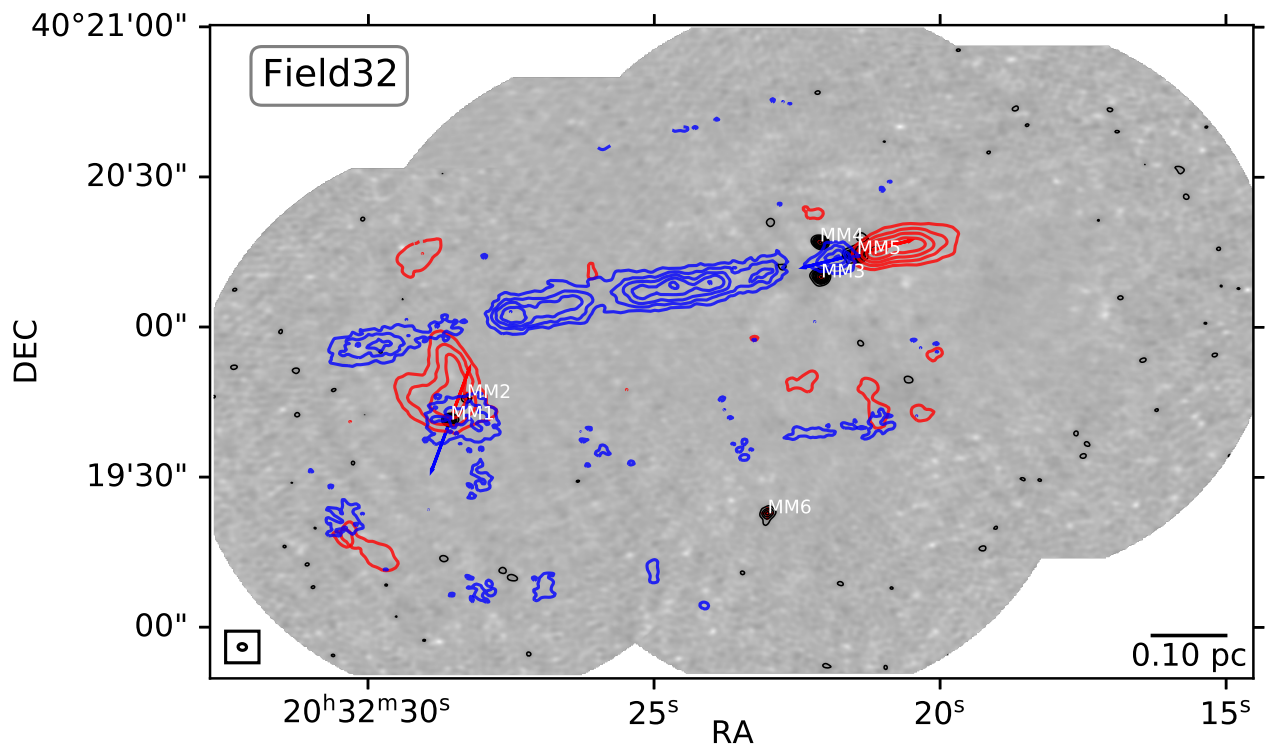


Fig. A.2. SMA CO outflow maps of DR15. Similar to Fig 2

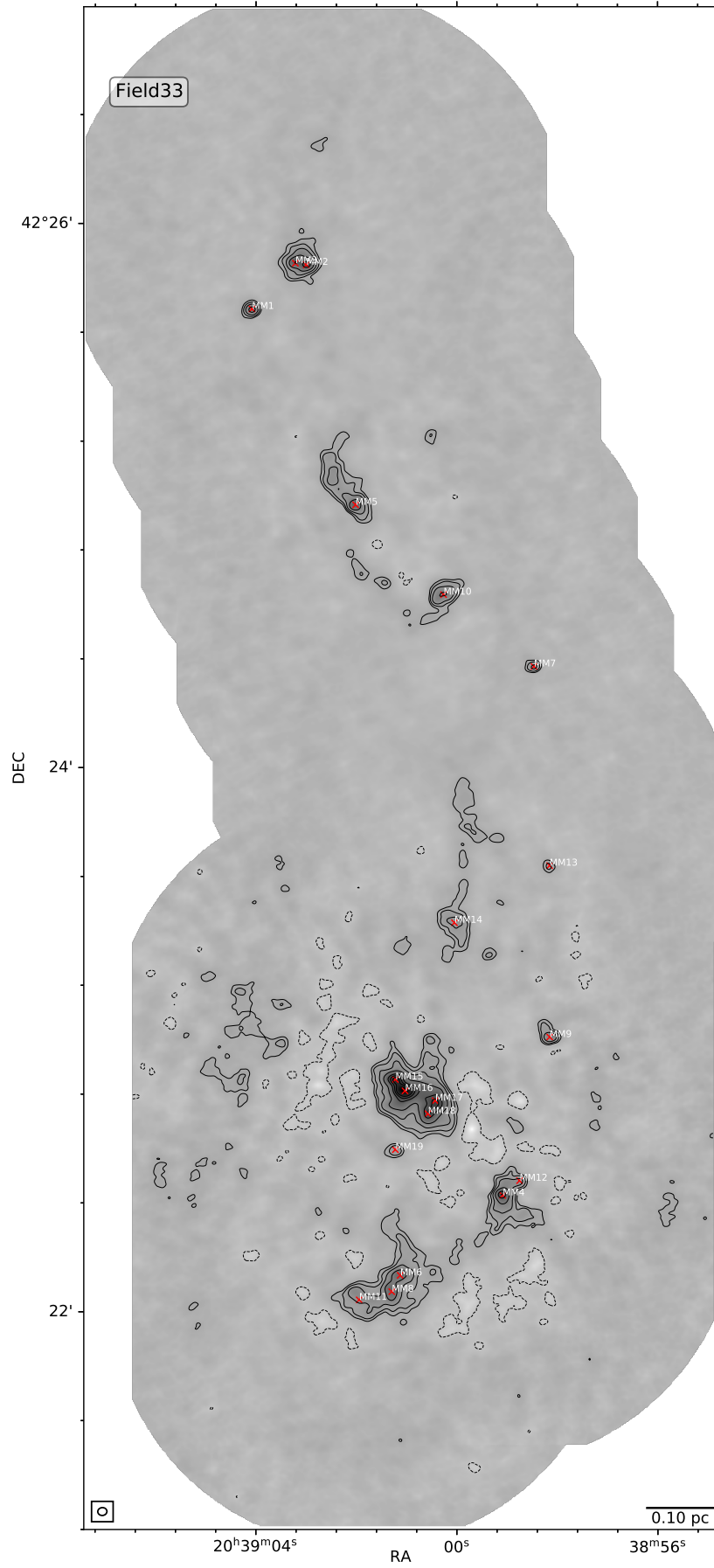


Fig. A.3. SMA 1.3 mm continuum map of DR21OH. Similar to Fig 1

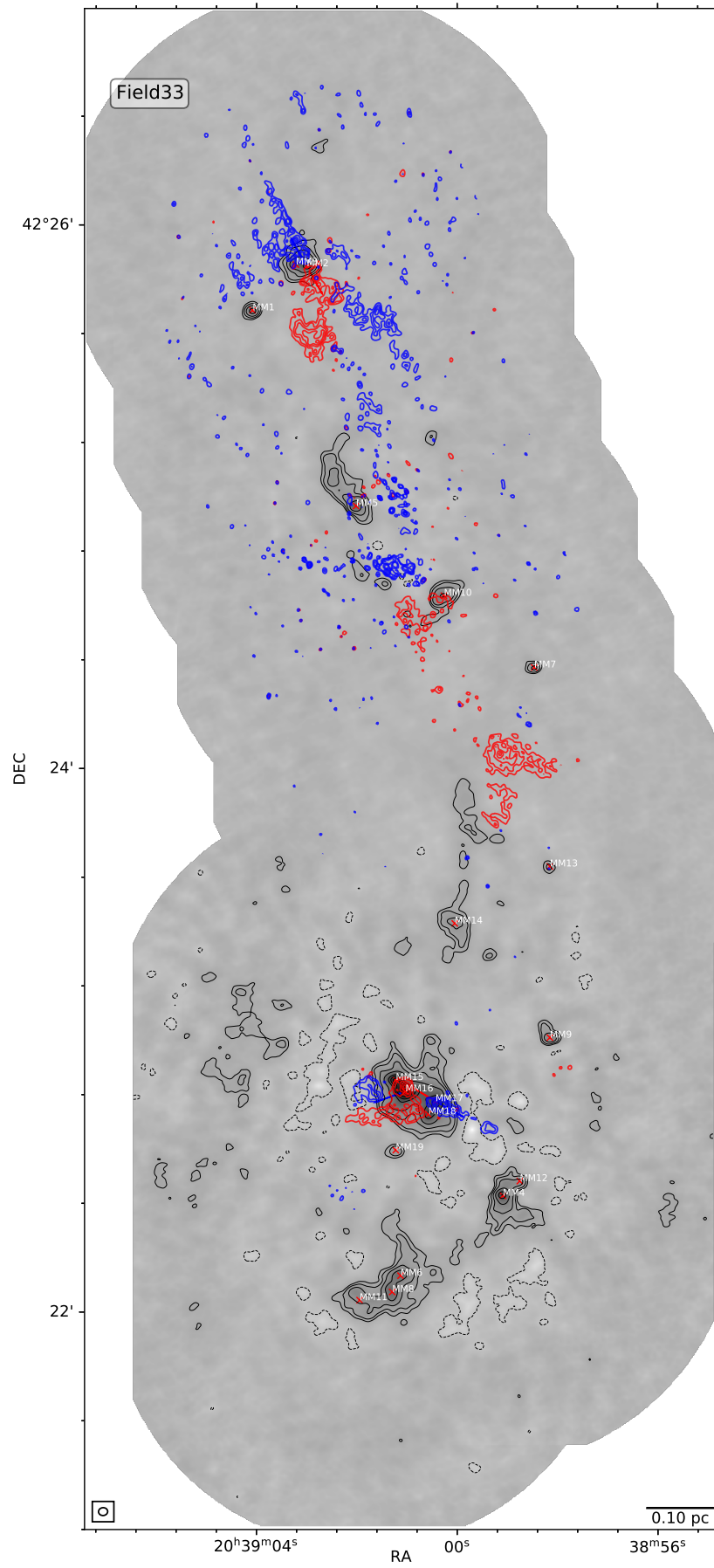


Fig. A.4. SMA CO outflow maps of DR21OH. Similar to Fig 2

Appendix B: Gas temperature

We detected several components of $\text{CH}_3\text{CN}(12_k - 11_k)$ k-ladder (listed in Table 2) in a few sources in our sample. The $\text{CH}_3\text{CN}(12_k - 11_k)$ level is helpful in temperature estimates. The three transitions of H_2CO with rest frequencies of 218.222, 218.475, and 218.760 GHz can also be used for estimations of temperature since they are strong and can be fitted simultaneously within a single spectral window in our SMA observations. We have carefully checked the potential influence of absorption and outflow on temperature estimates with H_2CO emission. We used the XCLASS (eXtend CASA Line Analysis Software Suite) tool (Möller et al. 2017) to fit the lines for temperature estimates. The myXCLASS function in XCLASS models a spectrum by solving the radiative transfer equation for an isothermal object in one dimension. For example, Fig B.1 shows the fitting results of $\text{CH}_3\text{CN}(12_k - 11_k)$ and H_2CO in Field5 MM1. The derived gas temperatures are listed in Table B.1. Sources that have H_2CO emission affected by outflows are marked by asterisks. It is worth noting that the gas temperatures estimated from transitions of CH_3CN and H_2CO are higher than the dust temperature from Cao et al. (2021). Because of our coarse resolution, the emission of dense gas tracers, especially CH_3CN , probably mainly comes from the inner, unresolved structure surrounding the protostar, which is denser and hotter. It could make the gas temperatures derived from these dense gas tracers much higher than the dust temperatures.

Table B.1 also includes NH_3 gas temperatures from Zhang et al. (2023). Their VLA 1.3 cm observations on Cygnus-X cover some MDCs in our SMA observations. They used the lowest NH_3 transitions, $\text{NH}_3(1, 1)$ and $(2, 2)$, to estimate the rotational temperature. Their angular resolution was sufficient (about $3''$) to distinguish two individual condensations.

It is important to note that only a few condensations associated with outflow possess multiple transitions of CH_3CN and H_2CO for the temperature estimate and many sources have no NH_3 gas temperature from Zhang et al. (2023). Consequently, a comprehensive comparison of gas temperatures between disks and non-disks, like what we did with dust temperature, cannot be achieved.

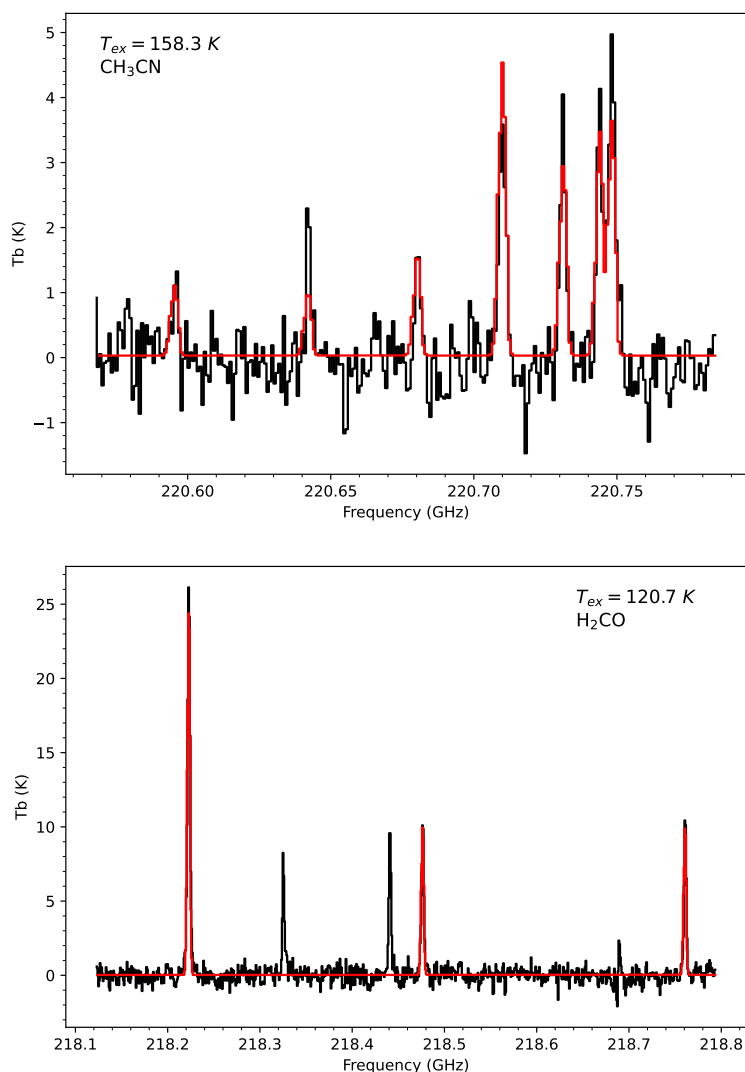


Fig. B.1. XCLASS fitting results of CH_3CN and H_2CO toward Field5 MM1. The black lines represent line emission averaged in the FWHM of the condensation. The red lines are the fitting results from XCLASS. The derived gas temperature from XCLASS is labeled in the map.

Table B.1. Estimation of molecular gas temperature

Condensation	$T_{\text{CH}_3\text{CN}}^a$ (K)	$T_{\text{H}_2\text{CO}}^a$ (K)	$T_{\text{NH}_3}^b$ (K)	T_d (K)	Group
Field3 MM1	...	94*	...	40	Disk Candidate
Field4 MM1	136	194*	38	37	Disk Candidate
Field5 MM1	158	121*	31	31	Disk Candidate
Field7 MM2	182	111*	110	35	Disk Candidate
Field8 MM1	...	88*	25	40	Disk Candidate
Field9 MM1	172	147*	...	17	Disk Candidate
Field16 MM1	197	364*	...	32	Disk Candidate
Field18 MM1	27	27	Disk Candidate
Field21 MM1	...	121*	24	34	Disk Candidate
Field1 MM1	...	63*	...	18	Dense-Gas-Traced
Field1 MM2	...	74*	40	25	Dense-Gas-Traced
Field4 MM3	...	173*	30	18	Dense-Gas-Traced
Field10 MM3	20	18	Dense-Gas-Traced
Field11 MM1	...	103*	33	37	Dense-Gas-Traced
Field12 MM1	22	Dense-Gas-Traced
Field14 MM1	42	Dense-Gas-Traced
Field17 MM3	...	69*	20	21	Dense-Gas-Traced
Field22 MM2	...	70*	17	18	Dense-Gas-Traced
Field23 MM1	14	26	Dense-Gas-Traced
Field26 MM1	21	Dense-Gas-Traced
Field29 MM2	23	Dense-Gas-Traced
Field32 MM1	43	Dense-Gas-Traced
Field32 MM5	16	Dense-Gas-Traced
Field33 MM2	...	15*	...	37	Dense-Gas-Traced
Field33 MM3	...	16*	...	18	Dense-Gas-Traced
Field33 MM16	...	280*	...	35	Dense-Gas-Traced
Field33 MM17	...	18*	...	27	Dense-Gas-Traced
Field2 MM4	42	Outflow-Associated
Field3 MM2	21	24	Outflow-Associated
Field6 MM2	17	16	Outflow-Associated
Field8 MM3	17	Outflow-Associated
Field10 MM2	23	Outflow-Associated
Field10 MM4	26	Outflow-Associated
Field11 MM3	23	Outflow-Associated
Field14 MM2	16	18	Outflow-Associated
Field17 MM4	19	Outflow-Associated
Field17 MM5	22	Outflow-Associated
Field17 MM8	18	42	Outflow-Associated
Field18 MM3	15	20	Outflow-Associated
Field20 MM2	22	Outflow-Associated
Field21 MM3	24	30	Outflow-Associated
Field21 MM4	35	Outflow-Associated
Field21 MM7	38	Outflow-Associated
Field22 MM3	18	Outflow-Associated
Field25 MM3	15	Outflow-Associated
Field26 MM2	21	Outflow-Associated
Field28 MM1	30	Outflow-Associated
Field28 MM2	28	Outflow-Associated
Field31 MM1	21	Outflow-Associated

Notes.^(a) Gas temperature derived by XCLASS.^(b) Ammonia temperature from Zhang et al. (2023).^(*) H₂CO emission affected by outflows.